

## High-Flux Femtosecond X-Ray Emission from Controlled Generation of Annular Electron Beams in a Laser Wakefield Accelerator

T. Z. Zhao,<sup>1,2</sup> K. Behm,<sup>1,2</sup> C. F. Dong,<sup>3</sup> X. Davoine,<sup>4</sup> S. Y. Kalmykov,<sup>5</sup> V. Petrov,<sup>2</sup> V. Chvykov,<sup>1</sup> P. Cummings,<sup>1,2</sup> B. Hou,<sup>1</sup> A. Maksimchuk,<sup>1</sup> J. A. Nees,<sup>1</sup> V. Yanovsky,<sup>1</sup> A. G. R. Thomas,<sup>1,2</sup> and K. Krushelnick<sup>1,2</sup>

<sup>1</sup>*Center for Ultrafast Optical Science, University of Michigan, Ann Arbor, Michigan 48109, USA*

<sup>2</sup>*Nuclear Engineering and Radiological Sciences, University of Michigan, Ann Arbor, Michigan 48109, USA*

<sup>3</sup>*Princeton Plasma Physics Laboratory, Princeton University, Princeton, New Jersey, USA*

<sup>4</sup>*CEA DAM DIF, Bruyères-le-Châtel, 91297 Arpajon, France*

<sup>5</sup>*Department of Physics and Astronomy, University of Nebraska–Lincoln, Lincoln, Nebraska 68588-0299, USA*

(Received 3 September 2015; revised manuscript received 21 June 2016; published 24 August 2016)

Annular quasimonoenergetic electron beams with a mean energy in the range 200–400 MeV and charge on the order of several picocoulombs were generated in a laser wakefield accelerator and subsequently accelerated using a plasma afterburner in a two-stage gas cell. Generation of these beams is associated with injection occurring on the density down ramp between the stages. This well-localized injection produces a bunch of electrons performing coherent betatron oscillations in the wakefield, resulting in a significant increase in the x-ray yield. Annular electron distributions are detected in 40% of shots under optimal conditions. Simultaneous control of the pulse duration and frequency chirp enables optimization of both the energy and the energy spread of the annular beam and boosts the radiant energy per unit charge by almost an order of magnitude. These well-defined annular distributions of electrons are a promising source of high-brightness laser plasma-based x rays.

DOI: 10.1103/PhysRevLett.117.094801

Relativistic plasma waves driven by an intense laser pulse propagating through a low-density plasma can produce accelerating gradients orders of magnitude higher than those typically available from conventional solid-state accelerating structures [1–3]. Operating these laser plasma accelerators in the blowout regime [4] has made it possible to generate quasimonoenergetic, GeV-scale electron bunches that produce ultrabright, pulsed synchrotron x rays [5–9]. In this regime, plasma waves propagate at near-luminous speed and evolve synchronously with the optical driver, readily trapping initially quiescent background electrons [10]. The self-injection process (which defines the beam phase space structure) can thus be controlled by modifying the drive pulse parameters, such as chirping the frequency [11], shaping the pulse temporal profile [12], and changing the focusing geometry [13–15]. This process can also be accomplished by tailoring the plasma density profile. Specifically, self-injection can be localized to a region in space by introducing density gradients along the laser pulse propagation path [14,16]. These gradients affect the evolution of the wave buckets and can be used to minimize the electron beam energy spread [17–20].

In this Letter, we demonstrate a unique example of electron beam phase space control that relies on both density profile modification (i.e., introduction of a density down ramp and tailoring the electron density in both stages of the gas cell) as well as manipulation of the drive pulse parameters (i.e., varying the pulse length while

simultaneously introducing a positive frequency chirp). As a result, we observe electron beams composed of two components: a collimated axial beam with a continuous energy spectrum and a quasimonoenergetic annular beam carrying up to 20% of the total charge. The experiments also reveal almost an order of magnitude increase in the total energy of the emitted x rays per unit charge when the annular feature is present. This opens a route to increasing the brightness and the flux of compact x-ray sources relative to other plasma-based schemes [8,9,21,22]. An explanation for the creation of annular electron beams in laser wakefield acceleration experiments was given in Ref. [23] using simulations conducted with a uniform density prole consisting of an initially neutral mixture of 98%/2% He/N<sub>2</sub> gas. The formation of the annulus is attributed to self-injection into the second bucket of the wake, decay of the second bucket in the course of drive pulse depletion, and partial capture of released electrons by toroidal focusing pockets around the first bucket. In our experiments we have found that such annular beams can also be produced due to plasma wake elongation along a density down ramp. In this scenario, the annular beam electrons are injected into the wakefield bubble, along the down ramp, where they are then subjected to the accelerating and focusing fields of the cavity.

The experiments were performed using the 800 nm Ti:sapphire HERCULES laser facility at the University of Michigan. Figure 1 shows the experimental setup. The laser beam, delivering up to 3.0 J on target, was focused using

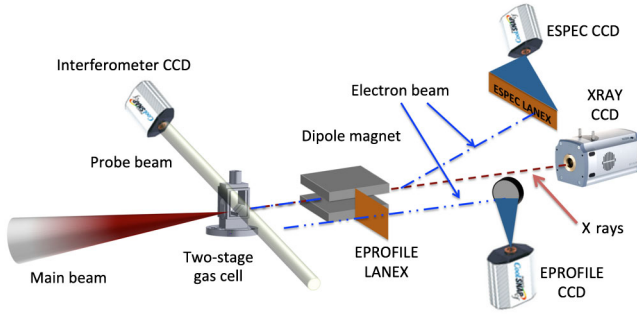


FIG. 1. Schematic of the experimental setup. The main beam is focused using an  $f/20$  off-axis paraboloid onto a two-stage gas cell. Electrons exiting the cell were either swept by a dipole magnet and imaged using the ESPEC diagnostic or undeflected and imaged on axis at 12 cm from the cell exit using the EPROFILE diagnostic (with the magnet removed in this case). The dash-double-dotted line shows the trajectory of the undeflected electrons.

an  $f/20$  off-axis paraboloid to a vacuum beam waist  $w_0 = 26 \mu\text{m}$  (at  $1/e^2$  of peak intensity). Second-order autocorrelation yielded a 34 fs duration of the fully compressed pulse (full width at half maximum in intensity) at the diagnostic. Decreasing separation of the compressor gratings stretched the pulse, while simultaneously imparting a positive frequency chirp. On-target peak intensities were thus on the order of  $10^{19} \text{ W/cm}^2$ . A 3D-printed two-stage gas cell was used as the target [24]. The cell was composed of a 1 mm higher-density injection stage, a 0.5 mm divider slit for stage separation, and an adjustable 5–10 mm low-density acceleration stage.

The experiments were conducted with the first stage filled with either pure helium or a mixed gas (97.5% He and 2.5%  $\text{N}_2$ ) [25,26]. The majority of shots were made with the mixed gas in the first stage. Observations, however, showed no evidence that the chemical composition of the first stage gas was essential in generating the annular beams. The second stage was always filled with pure helium. The energy spectra of both the axial and annular electron beams were measured using an electron spectrometer (ESPEC) which consisted of a 15 cm long, 0.8 T dipole magnet in conjunction with a LANEX screen and a 12-bit CCD camera. In addition, the spatial profile of the electrons was measured using an electron profile (EPROFILE) system consisting of a different LANEX screen positioned 12 cm from the exit of the gas cell and shielded from the laser light with 100  $\mu\text{m}$  of Cu foil. X-ray measurements were conducted using an Andor iKon-M BR-DD camera placed 2.5 m downstream from the interaction region and shielded from the laser light using two layers of 1.8  $\mu\text{m}$  Al and a 6  $\mu\text{m}$  aluminized Mylar foil. A 2  $\mu\text{m}$  thick nitro-cellulose pellicle reflected 4% of the main beam and was used to probe the gas cell in the transverse direction before entering a shearing Michelson interferometer, thus allowing electron density measurements to be taken. The use of

microscope glass slides in place of the printed plastic walls allowed the probe beam to access each stage of the gas cell. Density measurements could not be obtained in the region between the two stages due to the printed plastic wall obstructing the view.

The annular beams were generated for densities in both stages ranging from 2 to  $8 \times 10^{18} \text{ cm}^{-3}$ , laser energy between 2.4 and 3.0 J, acceleration stage length ranging from 5 to 9.5 mm, and pulse duration between 34 and 135 fs. Optimal combinations of these parameters yielded the annular beams in approximately 40% of shots. When the annular beams were present, the ratio of the electron density in the first stage relative to the second stage was always greater than unity (1.4 on average). Thus, the presence of a down ramp between the stages was a key ingredient in forming the annular feature. The density value in each stage also affected the appearance of the annular beams. Instabilities in creating the annular beams are, most likely, due to changes in the plasma density in each stage of the gas cell (10% shot-to-shot variation) and shot-to-shot fluctuations in the laser beam parameters.

In the series of shots corresponding to Figs. 2 and 3, the average electron density in the injection (acceleration) stage was approximately 6 to  $7.5 \times 10^{18} \text{ cm}^{-3}$  (4 to  $5 \times 10^{18} \text{ cm}^{-3}$ ). Figures 2(a)–2(c) show the full angle divergence of the undeflected beams for three different lengths of the acceleration stage. Divergence of the axial beam remained nearly constant at approximately 20 mrad as the acceleration stage length increased by 4 mm. At the same time, the divergence of the annular beam decreased by a factor of 2 [cf. Fig. 2(d)]. In Fig. 2(e), the divergence of the annular beam is observed to decrease as its energy (calculated in the center plane of the ring along the dispersion direction) increases.

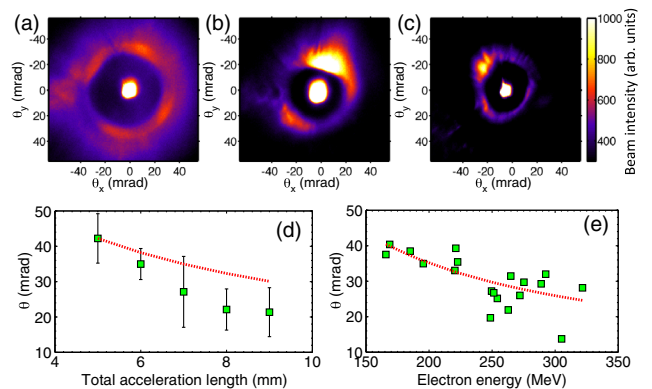


FIG. 2. (Top row) Images of the undeflected two-component beams taken 12 cm from the cell exit. The length of the acceleration stage is (a) 6, (b) 7, and (c) 8 mm. (d) and (e) indicate that the angle of conical emission decreased as either the acceleration length or the energy of the annular beam increased. The dashed lines show the momenta scalings described in Ref. [22]. Error bars in (d) denote the standard deviation.

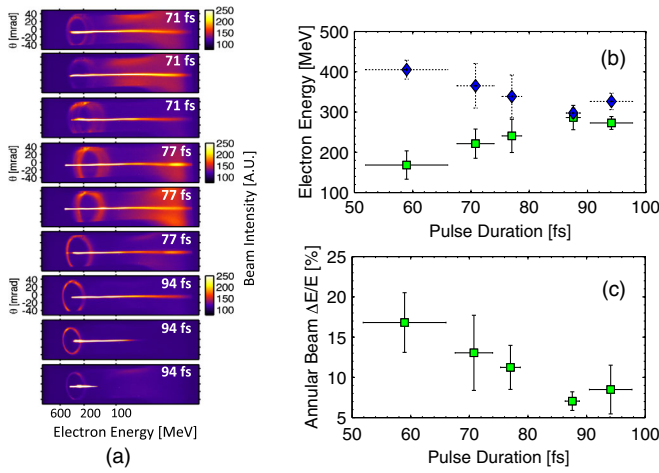


FIG. 3. (a) ESPEC images show the trend toward production of the most distinct, highest-energy annular beams as the pulse duration increases as well as their monoenergetic nature. (b) Increasing the pulse duration (while simultaneously imparting a positive frequency chirp) boosts the energy of the annular beams (square markers) while decreasing the maximum energy of the axial beam (the diamond markers). (c) The energy spread of the annular beams decreases as the pulse duration increases, reaching a minimum of approximately 7%.

The pulse duration corresponding to Figs. 2(d) and 2(e) was fixed at 34 fs, with an average laser energy of 2.7 J. This gives an estimated dephasing (pump depletion) length of approximately 3.2 (4.4) mm [27]. Thus, both components of the beam have propagated past the dephasing and depletion lengths. In consequence, both components of the beam initially gain energy in a laser-driven wakefield during the first half of the plasma. In the rear half of the plasma, the axial beam drives a plasma afterburner (i.e., a beam-driven wake) and is responsible for accelerating the annular component. This necessarily delays dephasing of the annular beam and causes its continuous acceleration through the entire plasma [28,29]. In addition, the injection of the annular electrons occurs during the laser wakefield acceleration process, before the second stage, since the wakefield becomes beam driven shortly afterwards. In this case, Figs. 2(d) and 2(e) can be explained by considering the motion of an electron in phase space inside the wakefield bubble. After being trapped at the rear of the bubble, an electron undergoes transverse oscillations that resemble simple harmonic motion with a slowly varying frequency if its acceleration time is long compared with its oscillation period. Since this frequency is slowly varying, there exists an adiabatic invariance that is the conservation of the area enclosed in phase space [30]. By using the Wentzel-Kramers-Brillouin approximation to solve for the equations of motion, one can then deduce that  $p_{\perp}$ , the transverse momentum, is proportional to  $\gamma^{1/4}$ . The electron will also have a longitudinal momentum,  $p_{\parallel} \propto \gamma$  [22]. The ratio of the transverse to longitudinal momenta is

then proportional to  $\gamma^{-3/4}$ . Thus, as the electrons are accelerated to higher energies, their angular spread will necessarily decrease. This scaling, shown by the dashed line in Figs. 2(d) and 2(e), corroborates the experimental data. The annular beam also maintains its monoenergetic nature after propagating over distances up to 3 times the dephasing length, while the axial beam has a very broad energy distribution, as would be expected. These observations show that the acceleration of the annular beam is due to a plasma afterburner instead of a laser-driven wake.

Figures 3(a)–3(c) demonstrate the effect of the laser pulse parameters on the mean energy and the energy spread of the annuli (defined as an average thickness of the annular shell along the dispersion direction). It should be mentioned that stretching the pulse imparts a frequency chirp and can change the pulse shape as well. Measurements of the pulse shape, conducted using the technique of frequency-resolved optical gating based on second harmonic generation [31], showed that the leading edge for positively chirped pulses is steeper compared with negatively chirped pulses but comparable to that of an optimally compressed pulse. In all of the presented cases, the chirp is positive.

Several important conclusions can be drawn from these figures. Figure 3(a) shows electron beams dispersed by the dipole magnet. The annular distribution is preserved after passing through the magnet, indicating the monoenergetic nature of these electrons. Furthermore, the energy of the annular beam remains below the maximum energy of the axial beam. Images in Fig. 3(a) also indicate that stretching the pulse trends toward production of the most distinct and highest-energy rings, with a significant drop in the axial signal. Studies have shown that a positive frequency chirp with a fast-rising leading edge can be used to increase the self-trapping of electrons by increasing the wakefield amplitude generated by the chirped pulse. The higher amplitude wakefield serves to decrease the minimum momentum necessary to trap electrons. In addition, frequency chirping affects the laser group velocity, which could then influence the injection process [12,32–34]. In our case, changing the pulse characteristics improved the energy and energy spread of the annulus but did not increase its charge. Data shown in Figs. 3(b) and 3(c) support this trend, indicating an increase in the mean energy of the annuli [the square markers in Fig. 3(b)]. In effect, as the pulse length increases, the energy of the annular component shifts toward the high-energy end of the axial-beam spectrum, while the energy spread of the annuli reduces [cf. Fig. 3(c)]. Although the longest pulse (94 fs) produced the most distinct rings, the rings were observed most consistently at a somewhat shorter (77 fs) pulse duration. Finally, the annular feature was always observed with an axial beam after the latter has propagated past the dephasing length. Attempts at generating the annular beam using longer, positively chirped pulses were unsuccessful due to an inability to generate the axial beam.

The effect of the annular beams on the x-ray flux was quantified by examining the ratio between the integrated counts on the x-ray camera and the integrated electron signal on the ESPEC LANEX. A direct comparison was then made between ESPEC images with and without the annular features using the corresponding x-ray images. The measurements were taken during the same shot run, with a laser energy of  $2.4 \pm 0.12$  J and all other parameters held fixed (except for the pulse duration). As shown in Fig. 4(a), the radiant energy per unit charge is higher when the annular beams are present in conjunction with the axial beam (the square markers), in contrast to the cases of the axial beam alone (the diamond markers). In particular, the radiant energy per unit charge increases by almost an order of magnitude for the pulse duration (94 fs), producing the most distinct, monoenergetic annuli. Figure 4(b) shows the x-ray spectra from both the axial plus annular (solid line) and axial-only beams (dash-dotted line) for the case of a 94 fs pulse duration, calculated using the method of single photon counting [35]. Corrections for predicted double hits based on Poisson statistics were made to the axial plus annular beam x-ray spectra due to the significant increase in radiation flux (with the annular beam present, the probability of a double hit ranged from 25%–35%) [36]. The axial-only beam spectrum is averaged over a minimum of nine shots, while the axial plus annular beam spectrum is constructed from a single shot.

The experimentally observed increase in the radiant energy in the presence of the annular beam is corroborated by a series of OSIRIS [37] simulations in which a 34 fs linearly polarized Gaussian pulse, with a  $0.8 \mu\text{m}$  carrier

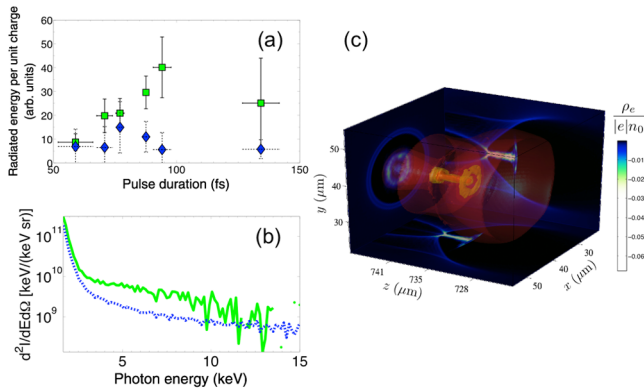


FIG. 4. (a) Presence of the annuli in conjunction with the axial beam increased the radiant energy per unit charge (the square markers) compared with cases of the axial beam alone (the diamond markers). At a pulse duration of 94 fs, the most distinct annular beams are responsible for almost an order of magnitude increase in the x-ray yield per unit charge. (b) Single photon spectrum of the axial plus annular (solid) and axial-only (dash-dotted) beams are shown for the case of a 94 fs pulse duration. (c) 3D map of charge density in the first bucket of the wakefield after the down ramp with both the axial and annular components of the electron beam (using OSIRIS).

wavelength and a waist size  $w_0 = 20 \mu\text{m}$  ( $a_0 = 2.2$ ,  $I \approx 10^{19} \text{ W/cm}^2$ ), is focused at the plasma entrance. In the simulations, the pure helium plasma begins with a  $64 \mu\text{m}$ -length linear density up ramp, followed by the  $573 \mu\text{m}$  plateau (first stage), then a  $64 \mu\text{m}$  linear down ramp (transition between the stages), and a  $255 \mu\text{m}$  low-density plateau (second stage). The density in the first stage is 0.175% of critical, with a 60% to 90% decrease along the down ramp. The set of charge-normalized synchrotron spectra from the simulations, obtained using recent modifications to the OSIRIS code [21,38], reveal that the presence of the annular beam can increase the flux for photon energies above 0.5 keV [39]. Since the spectra are normalized with respect to the electron charge, the increase in the flux of higher-energy photons is due to the large-amplitude transverse oscillations of the annular beam in the wakefield bubble rather than simply an increase in the injected charge. This increase is not observed for all simulated down ramp profiles, which is not inconsistent with the experimental observation that the annular beams do not always translate into an enhancement in the x-ray flux. For example, Fig. 4(a) shows that the x-ray enhancement is significant only at longer pulse durations (and positively chirped pulses). At 59 fs, the x-ray yield for the two cases are similar. In addition, Fig. 4(b) shows that the distinction in the spectra becomes more apparent at the higher photon energies.

The OSIRIS simulations used a  $76 \times 76 \times 86 \mu\text{m}^3$  box ( $x$ ,  $y$ , and  $z$  directions) with a longitudinal and transverse grid resolution of 25 and 6.3 cells per laser wavelength. The box clips the beam at  $x = y = \pm 1.9w_0$  and effectively creates a transversely non-Gaussian beam that can change the pattern of nonlinear focusing and seed transient filamentation. The latter sets up transverse density perturbations along the down ramp, causing transverse injection of a group of electrons in the shape of an annulus; see Fig. 4(c). This injection pattern persists for a range of densities in the second stage. By increasing the box size, and thus returning to a Gaussian beam without filamentation, the annulus is eliminated; this is supported by high-fidelity quasicylindrical 3D particle-in-cell simulations using CALDER-CIRC [40,41]. The mildly non-Gaussian pulse shape is not incompatible with the measured pulse shape and may thus account for the generation of the annuli in a broad parameter range.

In conclusion, we demonstrate almost an order of magnitude increase in the radiant energy per unit charge resulting from the localized injection of a group of electrons in the shape of an annulus from a laser wakefield accelerator and the subsequent acceleration in a plasma afterburner. Experimental data indicate that the monoenergetic annular beams are always accompanied by a high-charge collimated axial electron beam, and they have energy in the hundreds of MeV. The energy and energy spread of the annular beams were favorably modified using positively

chirped, longer duration pulses, resulting in an order of magnitude increase in the measured x-ray emission. The monoenergetic nature and phase space distribution of these electrons, along with the associated increase in emitted radiation, can be useful for applications in accelerator science where a high x-ray flux per unit charge is required.

This work is supported by U.S. Department of Energy/National Nuclear Security Administration Grant No. DE-NA0002372, National Science Foundation Career Grant No. 1054164, and Air Force Office of Scientific Research Young Investigator Program Grant No. FA9550-12-1-0310. The work of S. Y. K. has been supported by the National Science Foundation Grant No. PHY-1535678. The authors would like to acknowledge the OSIRIS consortium for use of the OSIRIS2.0 framework.

- 
- [1] E. Esarey, C. B. Schroeder, and W. P. Leemans, *Rev. Mod. Phys.* **81**, 1229 (2009).
- [2] V. Malka, *Phys. Plasmas* **19**, 055501 (2012).
- [3] D. A. Edwards and M. J. Syphers, *An Introduction to the Physics of High Energy Accelerators* (Wiley-VCH, Weinheim, 2004).
- [4] A. Pukhov, and J. Meyer-ter-Vehn, *Appl. Phys. B* **74**, 355 (2002).
- [5] C. McGuffey *et al.*, *Phys. Plasmas* **19**, 063113 (2012).
- [6] X. Wang *et al.*, *Nat. Commun.* **4**, 1988 (2013).
- [7] W. P. Leemans *et al.*, *Phys. Rev. Lett.* **113**, 245002 (2014).
- [8] S. Kneip *et al.*, *Appl. Phys. Lett.* **99**, 093701 (2011).
- [9] S. Corde, K. Ta Phuoc, G. Lambert, R. Fitour, V. Malka, A. Rousse, A. Beck, and E. Lefebvre, *Rev. Mod. Phys.* **85**, 1 (2013).
- [10] S. Y. Kalmykov, A. Beck, S. A. Yi, V. N. Khudik, M. C. Downer, E. Lefebvre, B. A. Shadwick, and D. P. Umstadter, *Phys. Plasmas* **18**, 056704 (2011).
- [11] S. Y. Kalmykov, A. Beck, X. Davoine, E. Lefebvre, and B. A. Shadwick, *New J. Phys.* **14**, 033025 (2012).
- [12] X. Zhang, B. Shen, L. Ji, W. Wang, J. Xu, Y. Yu, L. Yi, X. Wang, N. A. M. Hafz, and V. Kulagin, *Phys. Plasmas* **19**, 053103 (2012).
- [13] A. G. R. Thomas *et al.*, *Phys. Rev. Lett.* **98**, 095004 (2007).
- [14] A. J. Gonsalves *et al.*, *Nat. Phys.* **7**, 862 (2011).
- [15] S. Banerjee *et al.*, *Phys. Rev. ST Accel. Beams* **16**, 031302 (2013).
- [16] Z.-H. He, B. Hou, J. A. Nees, J. H. Easter, J. Faure, K. Krushelnick, and A. G. R. Thomas, *New J. Phys.* **15**, 053016 (2013).
- [17] C. G. R. Geddes, K. Nakumura, G. R. Plateau, Cs. Toth, E. Cormier-Michel, E. Esarey, C. B. Schroeder, J. R. Cary, and W. P. Leemans, *Phys. Rev. Lett.* **100**, 215004 (2008).
- [18] A. Buck *et al.*, *Phys. Rev. Lett.* **110**, 185006 (2013).
- [19] F. Y. Li, Z. M. Sheng, Y. Liu, J. Meyer-ter-Vehn, W. B. Mori, W. Lu, and J. Zhang, *Phys. Rev. Lett.* **110**, 135002 (2013).
- [20] D. Kaganovich, D. F. Gordon, M. H. Helle, and A. Ting, *J. Appl. Phys.* **116**, 013304 (2014).
- [21] S. Kiselev, A. Pukhov, and I. Kostyukov, *Phys. Rev. Lett.* **93**, 135004 (2004).
- [22] A. G. R. Thomas, *Phys. Plasmas* **17**, 056708 (2010).
- [23] B. B. Pollock *et al.*, *Phys. Rev. Lett.* **115**, 055004 (2015).
- [24] M. Vargas *et al.*, *Appl. Phys. Lett.* **104**, 56704 (2014).
- [25] C. McGuffey *et al.*, *Phys. Rev. Lett.* **104**, 025004 (2010).
- [26] A. Pak, K. A. Marsh, S. F. Martins, W. Lu, W. B. Mori, and C. Joshi, *Phys. Rev. Lett.* **104**, 025003 (2010).
- [27] W. Lu, M. Tzoufras, C. Joshi, F. S. Tsung, W. B. Mori, J. Vieira, R. A. Fonseca, and L. O. Silva, *Phys. Rev. ST Accel. Beams* **10**, 061301 (2007).
- [28] P. Dong *et al.*, *Phys. Rev. Lett.* **104**, 134801 (2010).
- [29] P. E. Masson-Laborde, M. Z. Mo, A. Ali, S. Fourmaux, P. Lasseigne, J. C. Kieffer, W. Rozmus, D. Teychenné, and R. Fedosejevs, *Phys. Plasmas* **21**, 123113 (2014).
- [30] I. Kostyukov, A. Pukhov, and S. Kiselev, *Phys. Plasmas* **11**, 5256 (2004).
- [31] K. W. DeLong and R. Trebino, *J. Opt. Soc. Am. A* **11**, 2429 (1994).
- [32] V. B. Pathak, J. Vieira, R. A. Fonseca, and L. O. Silva, *New J. Phys.* **14**, 023057 (2012).
- [33] S. P. D. Mangles, G. Genoud, M. S. Bloom, M. Burza, Z. Najmudin, A. Persson, K. Svensson, A. G. R. Thomas, and C.-G. Wahlström, *Phys. Rev. ST Accel. Beams* **15**, 011302 (2012).
- [34] W. P. Leemans, P. Catravas, E. Esarey, C. G. R. Geddes, C. Toth, R. Trines, C. B. Schroeder, B. A. Shadwick, J. van Tilborg, and J. Faur, *Phys. Rev. Lett.* **89**, 174802 (2002).
- [35] S. Fourmaux *et al.*, *New J. Phys.* **13**, 033017 (2011).
- [36] K. Behm, T. Z. Zhao *et al.* (to be published).
- [37] R. A. Fonseca *et al.*, in *Computational Science—ICCS 2002, Pt. III*, edited by P. M. A. Sloot, A. G. Hoekstra, C. J. K. Tan, and J. J. Dongarra, Lecture Notes in Computer Science Vol. 2331 (Springer, New York, 2002), p. 342.
- [38] P. Cummings *et al.* (to be published).
- [39] See Supplemental Material at <http://link.aps.org/supplemental/10.1103/PhysRevLett.117.094801> for calculated radiation spectra from OSIRIS.
- [40] A. F. Lifschitz, X. Davoine, E. Lefebvre, J. Faure, C. Rechatin, and V. Malka, *J. Comput. Phys.* **228**, 1803 (2009).
- [41] R. Lehe, A. Lifschitz, C. Thauray, V. Malka, and X. Davoine, *Phys. Rev. ST Accel. Beams* **16**, 021301 (2013).